



**HAL**  
open science

## **Ru exsolution in substituted La<sub>0.75</sub>Sr<sub>0.25</sub>Cr<sub>0.5</sub>Mn<sub>0.5</sub>O<sub>3-δ</sub> compound as anode material for an IT-SOFCs**

Léonard Thommy, M. Benamira, T. Jardiel, Veyis Gunes, O. Joubert, M.T.  
Caldes

### ► To cite this version:

Léonard Thommy, M. Benamira, T. Jardiel, Veyis Gunes, O. Joubert, et al.. Ru exsolution in substituted La<sub>0.75</sub>Sr<sub>0.25</sub>Cr<sub>0.5</sub>Mn<sub>0.5</sub>O<sub>3-δ</sub> compound as anode material for an IT-SOFCs. *Materials Chemistry and Physics*, 2021, 268, pp.124724. 10.1016/j.matchemphys.2021.124724 . hal-03270731

**HAL Id: hal-03270731**

**<https://hal.science/hal-03270731>**

Submitted on 13 Jun 2023

**HAL** is a multi-disciplinary open access archive for the deposit and dissemination of scientific research documents, whether they are published or not. The documents may come from teaching and research institutions in France or abroad, or from public or private research centers.

L'archive ouverte pluridisciplinaire **HAL**, est destinée au dépôt et à la diffusion de documents scientifiques de niveau recherche, publiés ou non, émanant des établissements d'enseignement et de recherche français ou étrangers, des laboratoires publics ou privés.



Distributed under a Creative Commons Attribution - NonCommercial 4.0 International License

## Ru exsolution in substituted $\text{La}_{0.75}\text{Sr}_{0.25}\text{Cr}_{0.5}\text{Mn}_{0.5}\text{O}_{3-\delta}$ compound as anode material for an IT-SOFCs

L. Thommy<sup>a</sup>, M. Benamira<sup>a,b,\*</sup>, T. Jardiel<sup>c</sup>, V. Günes<sup>d</sup>, O. Joubert<sup>a</sup>, M.T. Caldes<sup>a</sup>

<sup>a</sup>*Institut des Matériaux Jean Rouxel (IMN), Université de Nantes, 2, rue de la Houssinière, BP 32229, 44322 Nantes, France*

<sup>b</sup>*Laboratory of Interaction Materials and Environment (LIME), University of Jijel, Algeria*

<sup>c</sup>*Department of Electroceramics, Instituto de Cerámica y Vidrio (CSIC), C/Kelsen 5. Campus de Cantoblanco, 28049 Madrid, Spain*

<sup>d</sup>*Department of Oxides and Fluorides, Institute of Molecules and Materials Le Mans (IMMM) Université du Maine, Avenue Olivier Messiaen, 72085 Le Mans, France*

\*Corresponding author. [m\\_benamira@univ-jijel.dz](mailto:m_benamira@univ-jijel.dz), [maite.caldes@cnrs-imn.fr](mailto:maite.caldes@cnrs-imn.fr).

### Abstract

In this study, the synthesis of  $\text{La}_{0.75}\text{Sr}_{0.25}\text{Cr}_{0.4}\text{Mn}_{0.5}\text{Ru}_{0.1}\text{O}_{3-\delta}$  a ( $\text{LSC}_{0.4}\text{MRu}_{0.1}$ ) compound is presented and its total conductivity is measured and compared with that of  $\text{La}_{0.75}\text{Sr}_{0.25}\text{Cr}_{0.5}\text{Mn}_{0.5}\text{O}_{3-\delta}$  (LSCM) and the Ni-substituted compound  $\text{La}_{0.75}\text{Sr}_{0.25}\text{Cr}_{0.5}\text{Mn}_{0.3}\text{Ni}_{0.2}\text{O}_{3-\delta}$  ( $\text{LSCM}_{0.3}\text{Ni}_{0.2}$ ). While the substitution of Ni decreased LSCM conductivity under a reducing atmosphere, an increase of the total conductivity of Ru substituted phase is evidenced. The reduction of Ni and Ru-substituted LSCM under Ar/H<sub>2</sub> 5% up to 800 °C or 1000 °C respectively leads to the exsolution of nanoparticles, but also to a slight decomposition for the Ru-substituted compound. However, the use of these reduced materials as anode for solid oxide fuel cell (SOFC) in symmetrical cells based on Ce<sub>0.9</sub>Gd<sub>0.1</sub>O<sub>1.95</sub> (CGO) electrolyte implies not reducing the total system at a temperature higher than 600 °C to avoid ceria reduction. The solution consists of pre-reducing the electrode materials at their exsolution temperature before casting them on CGO thin disk. Under reductive atmospheres, Electrochemical impedance spectroscopy study of symmetrical cells suggests that the exsolution approach improves the adsorption of gaseous species compared to LSCM.  $\text{LSC}_{0.4}\text{MRu}_{0.1}$  symmetrical cell exhibits the lowest polarization resistance, 0.087  $\Omega\cdot\text{cm}^2$  under Ar/H<sub>2</sub> (5%) and 0.044  $\Omega\cdot\text{cm}^2$  under methane at 600 °C.

**Keywords:** SOFC anode, Exsolution, MIEC, LSCM, Symmetrical Cells.

## 1. Introduction

The development of Solid Oxide Fuel Cells (SOFC) to intermediate operating temperatures (500-700 °C) brings the scientific community to develop new concepts to keep the good performance of the devices [1-6]. It is particularly important to develop electrodes with increased activity towards oxygen reduction and fuel oxidation at these temperatures. Moreover, one of the main interests of SOFC is the direct use of carbonated fuels, thus leading to the development of Mixed Ionic and Electronic Conductors (MIEC) anode to replace the composite ones containing nickel. Indeed, the presence of a O<sub>2</sub>- mobility in the electrode material can be useful against coking and for direct hydrocarbon oxidation [7-11].

Electrochemical characteristics of ceramic electrodes can be enhanced by the addition of metallic (e.g. Nickel or Ruthenium) nanoparticles at the surface of the material [12-14]. It has also been proved useful to limit the coking effect due to hydrocarbon cracking when using carbonated fuels [15,16]. It is possible to add these particles as a second phase with processes such as impregnation of a metallic salt in the porous electrode structure. This process is usual in the field of reforming catalysis [12,17]. However, this method can lead to compositional inhomogeneities and particle coarsening [18]. Another way to obtain these nanoparticles is to substitute the metallic oxide in the ceramic phase and to induce the precipitation upon reduction. This technique, named exsolution, is known for several years in the field of SOFC, and has already been explored by substituting Ni or Ru in La<sub>0.8</sub>Sr<sub>0.2</sub>CrO<sub>3-δ</sub> (LSC) for example [19,20]. Recent papers have shown that this phenomenon is related to the stoichiometry of the different elements in the ceramic phase [21] and that it is observed not only on the surface but also in the bulk of the phase [22] and is potentially reversible [22,23]. The exsolved particles show a strong interaction with the support, which can lead to better stability [24], but also to a deactivation of the particles [25]. Moreover, it is often neglected that the supporting phase must retain its properties after metal departure from the bulk for certain applications such as SOFC. The lanthanum strontium chromo-manganite La<sub>0.75</sub>Sr<sub>0.25</sub>Cr<sub>0.5</sub>Mn<sub>0.5</sub>O<sub>3-δ</sub> (LSCM) was reported to be a promising anode material to replace Ni-YSZ cermet, demonstrating both good performances as a catalytic material for H<sub>2</sub> and CH<sub>4</sub> oxidation and redox stability in low steam to hydrocarbon ratios [26,27]. It is also considered as an efficient cathode material with performances comparable to several optimized LSM cathodes at temperatures as low as 650°C [28].

In IMN lab, we have reported the substitution of Mn or Cr by Ni in LSCM, leading to new phases exhibiting a dispersion of Ni nanoparticles at the surface of the crystallites after reduction, and improved catalytic activity [29]. In continuation of this work, the same approach has been considered with the substitution of Ru on the B-site of LSCM. Ru is explored as an alternative to Ni since it is less subject to sintering and coking [16]. This work will focus on the new  $\text{La}_{0.75}\text{Sr}_{0.25}\text{Cr}_{0.4}\text{Mn}_{0.5}\text{Ru}_{0.1}\text{O}_{3-\delta}$  ( $\text{LSC}_{0.4}\text{MRu}_{0.1}$ ) compound. First, the synthesis, structure and transport properties will be presented and compared to that of LSCM and  $\text{La}_{0.75}\text{Sr}_{0.25}\text{Cr}_{0.5}\text{Mn}_{0.3}\text{Ni}_{0.2}\text{O}_{3-\delta}$  ( $\text{LSCM}_{0.3}\text{Ni}_{0.2}$ ). Since these properties are linked to the oxidation states of the element, XPS analysis is also reported. The reduction of Ni- and Ru-substituted LSCM compounds are studied by in situ XRD and post-treatment scanning electron microscopy (SEM), putting emphasis on the exsolution process. An original way of fabricating CGO supported symmetrical cells was proposed which consisted of using pre-exsolved materials, in order to never expose CGO to temperature higher than 600 °C under reducing atmosphere. This fabrication process not only solves the phase deterioration problem of  $\text{LSC}_{0.4}\text{MRu}_{0.1}$  during exsolution but also might be considered as an original process to obtain nanostructured composites for electrodes with well-dispersed catalysts. We show that this process allows making high performance anodes without the need for using a treatment susceptible to reduce the ceria electrolyte.

In order to evaluate the applicability of such phases as fuel electrode in SOFC or Solid Oxide Electrolyzer Cells (SOEC), this paper ends with the evaluation of the polarization resistance ( $R_p$ ) of these cells under Ar/H<sub>2</sub> 5% and CH<sub>4</sub>, allowing us to discuss the interest of exsolution and the difference between Ni- and Ru-substituted compounds.

## 2. Experimental

Metal nitrates  $\text{La}(\text{NO}_3)_3 \cdot 9\text{H}_2\text{O}$ ,  $\text{Sr}(\text{NO}_3)_2$ ,  $\text{Cr}(\text{NO}_3)_3 \cdot 9\text{H}_2\text{O}$ ,  $\text{Mn}(\text{NO}_3)_2 \cdot 4\text{H}_2\text{O}$  and  $\text{Ru}(\text{NO})(\text{NO}_3)_3$  (Ru 1.5% w/v) purchased from Alfa Aesar (Purity > 99.0%) were used as received.  $\text{LSC}_{0.4}\text{MRu}_{0.1}$  powders were synthesized by combustion method, using citric acid as complexing agent and fuel. The metal nitrates were mixed with citric acid in ultrapure water. After evaporation, a gel is obtained and a combustion occurred. The resulting ashes were calcined at 800 °C during 2 hours, milled and then heat treated at 1000 °C for 12 hours to complete the reaction. For conductivity measurements, dense samples have realized using the raw powders, pressed into pellets and fired at 1450 °C during 60 hours.

CGO fine powder (crystallites <60 nm) was also synthesized by a self-combustion method using citric acid as fuel.  $\text{Ce}(\text{NO}_3)_3 \cdot 4\text{H}_2\text{O}$  and  $\text{Gd}(\text{NO}_3)_3 \cdot 4\text{H}_2\text{O}$  (Alfa Aesar, > 99%) were used as precursors. After evaporation and combustion, the precursor obtained was calcinated at 800 °C and ball milled at 500 rpm during 24 h. It was possible to obtain dense cylindrical pellets after sintering this powder at 1550 °C during 5 h.

XRD data were obtained using a Bruker “D8 Advance” powder diffractometer operating in Bragg-Brentano geometry with a Cu anode X-ray source, a focusing Ge(111) primary monochromator (selecting the Cu  $K_{\alpha 1}$  radiation) and a 1-D position-sensitive “Vantec” detector. The experimental data were treated using the FullProf program [30] and its graphical interface WinPLOTR.

High temperature X-ray diffraction (HTXRD) patterns were collected using a D8 Bruker diffractometer equipped with an Anton Paar XRK 900 Reactor Chamber and a Vantec1 linear detector, with the Cu  $K_{\alpha}$  radiation ( $\lambda = 1.54056 \text{ \AA}$ ) and  $2\theta$  varying from 20 to 90° by steps of 0.0146° and 0.4s counting time per step. Each pattern was collected in 30 min. Measurements were carried out between room temperature and 800°C every 50 °C, under wet air, dry and wet  $\text{H}_2$  flow on heating and cooling with a rate of 720 °C  $\text{h}^{-1}$  between each temperature step. For each temperature, the measurements were performed for 2 to 6 h to reach thermodynamic equilibrium (4 to 12 X-ray patterns per temperature, respectively). Gas humidification was performed by passing the gases through the water at room temperature.

Total conductivity measurements (4-probe DC) were carried out in a quartz tube heated in a tubular oven, on dense bars (compacity > 90%) cut from pellets, over which Au electrodes were deposited. Measurements were carried every 50 °C upon cooling at 50 °C  $\text{h}^{-1}$  between 850 °C and 200 °C, under air and wet  $\text{Ar}/\text{H}_2$  (5%).

The ionic conductivity has been evaluated by two electrode DC measurements with an electron-blocking microelectrode, with the method and setup described by Zipprich and Wiemhöfer [31]. 8YSZ microelectrode has been fabricated from a Tosoh© TZ-8Y powder, and sealed at the surface of a 1.5 mm thick, 8 mm wide pellet. Pt was painted at each extremity of the system (Fig. 1a). Assuming no ohmic loss in the sample due to its electronic conduction, the oxygen partial pressure at the surface of the micro-contact ( $P_{\text{O}_2}^{mc}$ ) is imposed by the applied voltage according to the Nernst equation:

$$U = \frac{RT}{4F} \ln \frac{P_{\text{O}_2}''}{P_{\text{O}_2}^{mc}} \quad (1)$$

where  $P_{\text{O}_2}''$  is the oxygen partial pressure at the Pt electrode deposited at YSZ surface (Fig. 1a).

The ionic conductivity ( $\sigma_{O^{2-}}(P_{O_2}^{mc})$ ) has been calculated in the hypothesis of a hemispherical contact according to the equation (2):

$$\sigma_{O^{2-}}(P_{O_2}^{mc}) = \frac{1}{2\pi a} \ln \frac{dI}{dU} \quad (2)$$

where  $a$  is the radius of the microelectrode of YSZ (50  $\mu\text{m}$ ).

XPS measurements were obtained with a Kratos AXIS Ultra spectrometer with a monochromatic Al  $K\alpha$  X-ray source (1486.6 eV), operating at 150 W. Quantification was performed using CasaXPS (CasaXPS © 2005 Casa Software Ltd) from the photoelectron peak areas using Shirley background subtraction. Spectra were calibrated in binding energy with C 1s assumed to be at 284.8 eV. The base pressure in the analysis chamber was  $10^{-8}$  Pa and the analyzed area was  $700 \times 300 \mu\text{m}^2$ . The hemispherical analyzer was used in Constant Analyzer Energy (CAE) mode for all spectra. The analysis of the 3s core level zone of manganese was carried out with a pass energy ( $E_p$ ) of 20 eV, while that of the 3p core level Ru was 40 eV.

Transmission Electron Microscopy (TEM) study was carried out with a Hitachi H9000NAR electron microscope, operating at 300 kV equipped with an energy dispersive X-ray (EDX) analyzer. The compounds were gently ground in ethanol and microcrystals were deposited on a holed carbon film supported by a copper grid. Scanning Electron Microscopy (SEM) was performed on a JEOL 7600 at low voltage.

EIS data were collected using a Solartron 1260 frequency response analyzer. The symmetrical cells were held between two golden disks in a tubular oven. The impedance spectra were recorded over a frequency range  $10^6$ - $10^{-2}$  Hz with 10 points per decade under open circuit conditions and wet ( $p(\text{H}_2\text{O}) = 0.025$  atm) reducing atmosphere (Ar/H<sub>2</sub> 5%) between 350 and 600 °C, every 50 °C. Two hours of stabilization time was considered between each temperature step. Impedance data was analyzed using Zview® software.

### **3. Results and discussion**

#### **3.1. Structural and transport properties of LSC<sub>0.4</sub>MRu<sub>0.1</sub>**

LSC<sub>0.4</sub>MRu<sub>0.1</sub> powder was synthesized by combustion method. EDX analysis gives the composition La<sub>0.76</sub>Sr<sub>0.24</sub>Cr<sub>0.40</sub>Mn<sub>0.51</sub>Ru<sub>0.091</sub>O<sub>3- $\delta$</sub> , very close to the expected stoichiometry, and phase adopts a rhombohedral structure (space group R $\bar{3}c$  (167), Fig. 1b), corresponding to the literature [25]. The reliability factors ( $\chi^2$ , R<sub>p</sub>, R<sub>w</sub>) of the refinement using the software Fullprof are 2.25, 8.03 and 11.9, respectively. Refined cell parameters, a = 5.4751(2) Å,  $\alpha$  = 60.609(6)° and V = 117.57(1) Å<sup>3</sup>, are slightly bigger than the previously reported values for LSCM: a = 5.4562(3) Å,  $\alpha$  = 60.440(9)°, V = 116.00(4) Å<sup>3</sup> [26]. This can be explained by the bigger size of Ru (IV) cation (0.62 Å) compared to Cr (0.615 Å) [32], suggesting the efficient substitution of Cr by Ru. Pellets with high density (> 95%) have been obtained after sintering at 1450 °C for 60 h.

The electrical conductivity of the Ru-substituted phase has been measured by 4 points DC on dense bars cut from pellets. The results are represented in Fig. 2 and compared to LSCM and LSCM<sub>0.3</sub>Ni<sub>0.2</sub> [29]. Under air at 600 °C, the total conductivity of LSC<sub>0.4</sub>MRu<sub>0.1</sub> is 14.5 S.cm<sup>-1</sup>, nearly three times higher than that of LSCM and LSCM<sub>0.3</sub>Ni<sub>0.2</sub> (Fig. 2a). Under reducing atmosphere, the conductivity level of the considered compositions decreases, down to 2.2 S.cm<sup>-1</sup> for LSC<sub>0.4</sub>MRu<sub>0.1</sub>, and around 0.1 S.cm<sup>-1</sup> for LSCM or LSCM<sub>0.3</sub>Ni<sub>0.2</sub> (Fig. 2b). These values and their variations along with the atmosphere are in agreement with previous results obtained for LSCM [27,33]. Our results suggest that Ru-doping at least favors a higher conductivity. The activation energies calculated for the conductivity of LSC<sub>0.4</sub>MRu<sub>0.1</sub> under air and wet Ar/H<sub>2</sub> (5%) range between 0.22 and 0.30 eV (Fig. S1). Since LSC<sub>0.4</sub>MRu<sub>0.1</sub> total conductivity decreases with p(O<sub>2</sub>) and that LSCM is a p-type conductor [33], it is fairly believable that electron holes are also the predominant charge carriers in LSC<sub>0.4</sub>MRu<sub>0.1</sub>. In all cases, the low E<sub>a</sub> corresponds to that of materials with a high electron transport number, since ion diffusion migration energy is most often much higher (close to 0.5 eV for protons, between 0.6 and 1 eV for oxygen anions). This hypothesis is supported by the fact that low ionic transport number, typically 10<sup>-4</sup>-10<sup>-6</sup>, have been measured for LSCM [33].

To evaluate this assessment, the oxide ion conductivity ( $\sigma_{O^{2-}}$ ) level of LSC<sub>0.4</sub>MRu<sub>0.1</sub> has been evaluated by two electrodes DC measurements with an electron-blocking microelectrode. Fig. 2c presents the oxide ion conductivity of LSC<sub>0.4</sub>MRu<sub>0.1</sub> as function of the oxygen activity at the microcontact.  $\sigma_{O^{2-}}$  reaches a maximum of 4 10<sup>-5</sup> S.cm<sup>-1</sup> at 600 °C or 700 °C and increases when the oxygen activity decreases. This could correspond to the creation of oxygen vacancies in the material structure during its reduction, increasing the charge carrier

concentration. At 600 °C, the small oxide ion transport number  $t_{\sigma O^{2-}} \approx 10^{-6}$ , confirms that  $\text{LSC}_{0.4}\text{MRu}_{0.1}$  is mostly electronic conductor at these temperatures.

The binding energy of the Mn 3s and Ru 3p<sub>3/2</sub> core level of Ru<sup>0</sup>, RuO<sub>2</sub>, LSCM,  $\text{LSC}_{0.4}\text{MRu}_{0.1}$  (in oxidized and reduced states), were measured by XPS in order to gain insight on the electric properties of the phase. They are presented in Fig. 3, while the values obtained are resumed in Table 1. Mn valence has been calculated from the 3s exchange-splitting ( $\Delta E_{3s}$ ) using a formula described in the literature [34]:

$$v_{Mn} = 9.67 - 1.27\Delta E_{3s} \quad (3)$$

The 3p<sub>3/2</sub> core level of Ru in  $\text{LSC}_{0.4}\text{MRu}_{0.1}$  in its oxidized state is higher than that in RuO<sub>2</sub>. Thus, its valence seems to be higher than 4. Mn valence in  $\text{LSC}_{0.4}\text{MRu}_{0.1}$  is lower than in LSCM. This indicates that the aliovalent substitution of Cr by Ru in these compounds seems to be compensated by the reduction of Mn<sup>4+</sup> to Mn<sup>3+</sup>. Under air, assuming that Mn and Ru are both able to be present at different oxidation state in the material ( $v_{Mn} > 3$ ) and not Cr, which retains strongly its six-fold coordination [26], it is possible to explain the increase in total conductivity when Cr is substituted by an increase of the potential charge carriers concentration.

Under Ar/H<sub>2</sub> (5%), Mn valence in  $\text{LSC}_{0.4}\text{MRu}_{0.1}$  decreases to reach approximatively 3. The total conductivity increase along with the Ru substitution seems to indicate that this element is still present in different oxidation state though the displacement of the 3p<sub>3/2</sub> core level of Ru measured by XPS suggest that this element is fairly reduced.

### 3.2. Characterization of $\text{LSCM}_{0.3}\text{Ni}_{0.2}$ and $\text{LSC}_{0.4}\text{MRu}_{0.1}$ reduction process

Thermal treatment at 800 °C in Ar/H<sub>2</sub> (5%) during 4DC measurements did not lead to the breaking of  $\text{LSCM}_{0.3}\text{Ni}_{0.2}$  and  $\text{LSC}_{0.4}\text{MRu}_{0.1}$  dense pellets and the measurement of their conduction properties does not reveal any decomposition of the material. Nevertheless, our previous experience shows that Ni-substituted powders could present exsolution in reducing atmosphere at temperatures close to 800 °C. We thus decided to explore the reduction process of  $\text{LSCM}_{0.3}\text{Ni}_{0.2}$  and  $\text{LSC}_{0.4}\text{MRu}_{0.1}$  powders. Ideally, the aim was to obtain exsolved particles without deterioration of the bulk structure, since electrocatalytic properties are linked to the kinetics of charge carriers' extraction and thus electric properties.

The reduction of  $\text{LSCM}_{0.3}\text{Ni}_{0.2}$  at 800 °C during 12 h under  $\text{Ar}/\text{H}_2$  (5%) induces a structural transition from a rhombohedral  $R\bar{3}c$  symmetry to a cubic  $\text{Pm}\bar{3}m$  one (Fig. 4a). HTXRD experiments under  $\text{N}_2/\text{H}_2$  (5%) indicate that the structural transformation occurs around 300 °C (Fig. 4b), though it does not imply that metallic Ni exsolves at this temperature. Indeed, Ni nanoparticles are observed at the surface of the grains after reduction at 800°C or above (Fig. 4c) [29]. This partial exsolution of nickel in the form of NiO is confirmed by TEM and SEM (Fig. 4d). EDX analysis are used to confirm the composition of the particles observed at the surface of the grains (inset, Fig. 4d).

The results of the Rietveld refinements carried out for  $\text{LSCM}_{0.3}\text{Ni}_{0.2}$  are presented in the Fig. S2 and the crystallographic characteristics gathered in the table S1.

Refinement of the cation and oxygen occupancy factors gives the composition  $\text{La}_{0.79}\text{Sr}_{0.21}\text{Cr}_{0.48}\text{Mn}_{0.32}\text{Ni}_{0.21}\text{O}_3$ , close to the nominal composition. A lower amount of nickel was observed in the reduced phase (0.17) compared to the oxidized phase (0.21). 0.04 mol / mole of  $\text{Ni}^{2+}$  or 19% of the nickel present in the phase is reduced to NiO which is exsolved at the surface.

It can be noted that the reduction of the compound induces an increase in the cell volume. The increase in volume is due to the change from a strongly distorted rhombohedral structure to a regular cubic structure. The  $B_{\text{iso}}$  of the elements in the reduced phase are higher than those observed for the oxidized phase, especially in the case of oxygen ( $3.29 \text{ \AA}^2$  for the reduced phase against  $0.73 \text{ \AA}^2$  for the oxidized phase). These results can be compared to those obtained by Tao and Irvine for LSCM ( $\text{La}_{0.75}\text{Sr}_{0.25}\text{Cr}_{0.5}\text{Mn}_{0.5}\text{O}_{3-\delta}$ ) [36] and displacement factors for oxygen  $B_{\text{iso}} = 0.82 \text{ \AA}^2$  for the oxidized phase and  $B_{\text{iso}} = 3.60 \text{ \AA}^2$  for the reduced phase.

Concerning  $\text{LSC}_{0.4}\text{MRu}_{0.1}$ , the thermal treatment of the powder under  $\text{Ar}/\text{H}_2$  (5%) induces the same structural transition from  $R\bar{3}c$  to  $\text{Pm}\bar{3}m$ , but HTXRD experiments indicated that this transition occurs at 800 °C, a much higher temperature than for  $\text{LSCM}_{0.3}\text{Ni}_{0.2}$  (Fig. 5a). However, reducing the compound at even 900 °C during 12 h is not sufficient to induce the exsolution of metallic particles on the surface.

Several attempts to observe exsolved particles on  $\text{LSC}_{0.4}\text{MRu}_{0.1}$  have been made at different temperatures from 800 °C to 1000 °C (Fig. 5b).  $\text{LSC}_{0.4}\text{MRu}_{0.1}$  has to be reduced at 1000 °C to observe a dispersion of Ru particles at the surface of the grains as shown by TEM and SEM images of the surface (Fig. 5c,d).

Together with the exsolution, a slight decomposition of the structure happens, and a  $(\text{La,Sr})_2(\text{Mn,Cr,Ru})\text{O}_4$  Ruddlesden-Popper type phase is observed by XRD. This phenomenon

is related to the role of non-stoichiometry for the exsolution process mentioned in the work done by J.T.S. Irvine group [21]. A-site non-stoichiometry would have been useful to exsolve Ru without damaging the bulk structure. Furthermore, Ru atom or cation is bigger than Ni, making it harder to diffuse out of the phase.

### **3.3. Preparation and electrochemical tests in symmetrical cells of Ni- and Ru-doped LSCM anodes**

The fabrication and EIS study of symmetrical cells is a process that implies heat treatments and exposition in different atmospheres, which may provoke some phase transformation and degradation. In order to study Ru-doped LSCM compounds with exsolved phases, we have had to adapt the fabrication process to avoid exposing the CGO electrolyte at 1000 °C under hydrogen atmosphere. Our objective was to propose a fabrication process as close as possible to the one for a complete cell. In this case, the reduction of CGO electrolyte has to be avoided to keep the integrity of the whole cell.

Cylindrical pellets of CGO have been sliced into 200-300 µm thick electrolytes with the help of a diamond string saw. No polishing was necessary. The electrode materials were then deposited by screen-printing. These materials were pre-exsolved powders for LSCM<sub>0.3</sub>Ni<sub>0.2</sub> and LSC<sub>0.4</sub>MRu<sub>0.1</sub>, meaning that they were treated under Ar/H<sub>2</sub> (5%) at 800 °C and 1000 °C respectively before being deposited. After sintering at 1150 °C, the electrode thickness was 20 µm, on top of which 10 µm of metallic Ni was screen-printed and sintered at 700 °C under N<sub>2</sub>. Following this approach, 3 different Ni/MIEC//CGO//MIEC/Ni symmetrical cells (MIEC : LSCM, LSC<sub>0.4</sub>MRu<sub>0.1</sub> or LSCM<sub>0.3</sub>Ni<sub>0.2</sub>) were obtained and thoroughly studied by EIS between 350 and 600 °C under wet Ar/H<sub>2</sub> (5%) (anodic conditions) in order to evaluate the influence of the metal chosen for the ex-solution approach.

In order to evaluate the influence of the cell fabrication and EIS study on LSCM<sub>0.3</sub>Ni<sub>0.2</sub> and LSC<sub>0.4</sub>MRu<sub>0.1</sub>, powders of these two exsolved materials were submitted to the same conditions in atmosphere controlled ovens and studied in XRD at each different step. The results are presented in Fig. 6.

While the first firing at 1150 °C induces a transition back to a rhombohedral symmetry, the reduction at 600 °C that corresponds to the conditions of the characterization induces the transition back into a cubic symmetry without observing the Ruddlesden-Popper phase. However, Ru particles were still observable at the surface of the electrode material after EIS experiments as will be shown thereafter. This allows us to discuss the properties of the

LSC<sub>0.4</sub>MRu<sub>0.1</sub> electrode with the light of the measurements previously presented in this study. It is also another proof of the complexity of the reversibility of the exsolution process. We use in this study the fact that we do not completely re-oxidize the phase material during the firing of the electrode.

The Nyquist plot at 600 °C of the three symmetrical cells are shown in Fig. 7, along with the equivalent circuit used to fit the impedance spectra, and subtracted from  $R_s$ .

$Rp_i$  and  $CPE_i$  are ohmic resistance and constant phase element of the phenomenon  $i$ . The (R-CPE)<sub>1</sub> and (R-CPE)<sub>2</sub> corresponds to the medium frequency arc (2300-3900 Hz) and the lower frequency arc (500-1300 Hz) respectively. The fit obtained with this model is in good agreement with experimental data for the 3 different cells at 600 °C under wet Ar/H<sub>2</sub>. Refined parameters, resistance, capacity and frequency are listed in Table 2.

Considering the characteristic frequencies of the two arcs, we assume that (R-CPE)<sub>1</sub> is associated to the charge transfer at the reactional interfaces, while (R-CPE)<sub>2</sub> is attributed to gas adsorption. The polarization resistance  $Rp$  mentioned afterwards is the sum of these processes, as an arc associable to gas diffusion is not always observable and will not allow the comparison of the results. The smallest  $Rp$  is observed for LSC<sub>0.4</sub>MRu<sub>0.1</sub> (0.087 Ω.cm<sup>2</sup>) while those of LSCM and LSCM<sub>0.3</sub>Ni<sub>0.2</sub> are equivalent (0.2 Ω.cm<sup>2</sup>). However, the low frequency arc resistance is smaller for LSCM<sub>0.3</sub>Ni<sub>0.2</sub> and LSC<sub>0.4</sub>MRu<sub>0.1</sub> ( $Rp_2 = 0.049$  and  $0.098$  Ω.cm<sup>2</sup>, respectively) than for LSCM ( $Rp_2 = 0.127$  Ω.cm<sup>2</sup>). Therefore, the exsolution process of Ni and Ru particles seems to influence gas adsorption.

Indeed, nanoparticles are observable on postmortem SEM images. Images of the cross-section of the Ni/LSCM//CGO//LSCM/Ni cell, along with the different cell's electrode, after EIS experiments, are shown in Fig. 8. The dense electrolyte is 200-300 μm thick and the porous electrode is composed of 20 μm of MIEC and <10 μm of Ni<sup>0</sup>. The interface between the electrode material and the electrolyte is correct, whereas the nickel current collector seems to be inconsistently connected at the top of the electrode layer. This can be related to the low sintering temperature used to attach the current collector and the post-mortem breaking of the cell necessary for obtaining such images. The electrode microstructure is porous and it is possible to observe Ni and Ru particles at the surface of LSCM<sub>0.3</sub>Ni<sub>0.2</sub> and LSC<sub>0.4</sub>Ru<sub>0.1</sub> grains, respectively.

Concerning EIS results, the slightly higher value of  $Rp_1$  observed for LSCM<sub>0.3</sub>Ni<sub>0.2</sub> (> LSCM > LSC<sub>0.4</sub>MRu<sub>0.1</sub>) can realistically be associated with the lower conductivity level of this phase in this environment (Fig. 2). The lower polarization resistances observed for the Ru-substituted material compared to that of the Ni-substituted one can be associated with a better

conductivity and gas adsorption due to the Ru-substituted bulk and nanoparticle properties. The  $R_p$  values of every cell evolve in a similar way with temperature (Fig. S3), following the Arrhenius law with an activation energy of 1.36-1.39 eV.

The  $R_p$  measured are low compared to those usually found for LSCM alone in the literature [26,37]. For example, Rath et al. [38] found a polarization resistance of  $0.247 \Omega \cdot \text{cm}^2$  under pure  $\text{H}_2$  at  $800 \text{ }^\circ\text{C}$  for symmetrical cells while using lanthanum doped ceria as electrolyte material but low frequency phenomena such as diffusion seem to be limiting their performances meaning that our electrode microstructure seems to be better. Table 4 presents the typical reported polarization resistance of A-site and B-site doped LSCM, STFNd and LSC anode materials.

### 3.4. Electrochemical tests in symmetrical cells under wet $\text{CH}_4$

To evaluate the interest of the substituted materials as MIEC anode material and the influence of the exsolved metal under methane,  $\text{LSC}_{0.4}\text{MRu}_{0.1}$  and  $\text{LSCM}_{0.3}\text{Ni}_{0.2}$ -based symmetrical cells (Differing from those presented before because a gold mesh was used as current collector) have been studied by EIS at  $600 \text{ }^\circ\text{C}$  under wet  $\text{CH}_4$ . Nyquist plots were fitted using the model as above. The calculated data are in good agreement with experimental data for the two cells (Fig. 9). Refined parameters, resistance, capacity and frequency are listed in Table 3. At  $600 \text{ }^\circ\text{C}$  under pure  $\text{CH}_4$ , symmetrical cells present  $R_p$  values lower than under  $\text{Ar}/\text{H}_2$  (5%), which can be the consequence of using a pure gas instead of diluted hydrogen. The  $\text{LSC}_{0.4}\text{MRu}_{0.1}$ -based cell presents the smallest  $R_p$  ( $0.044 \Omega \cdot \text{cm}^2$ ), once again due to a smaller  $R_{p1}$  and  $R_{p2}$ . It is interesting to observe that the ratio  $R_{p2}/R_{p1}$  increases for  $\text{LSCM}_{0.3}\text{Ni}_{0.2}$ -based symmetrical cell whereas it decreases for  $\text{LSC}_{0.4}\text{MRu}_{0.1}$ -based one. Consequently, the resistance to gas adsorption decreased even more for this cell. This is in agreement with the reported good catalytic activity of Ru towards  $\text{CH}_4$  [45]. Labhsetwar et al. [46] confirms the high thermal stability of Ruthenium when incorporated in perovskite type structure for high temperature applications like methane combustion.

## Conclusion

The electrode material LSCM has been successfully substituted with Ru on the B-site of the perovskite, in order to obtain a SOFC anode material with improved catalytic properties towards fuel oxidation. The new compound  $\text{LSC}_{0.4}\text{MRu}_{0.1}$ , presents a dispersion of Ru particles on the surface of its grain after reduction at 1000 °C, indicating partial exsolution of Ru from the phase, along with a slight deterioration. This is a significant difference with the reduction of  $\text{LSCM}_{0.3}\text{Ni}_{0.2}$ , a material previously developed with the same approach, which exsolves  $\text{Ni}^0$  upon reduction at 800 °C. The total conductivity of  $\text{LSC}_{0.4}\text{MRu}_{0.1}$  is mainly electronic and is much higher than that of  $\text{LSCM}_{0.3}\text{Ni}_{0.2}$  and LSCM. An original way of fabricating CGO supported symmetrical cells was proposed based on the partial irreversibility of the reduction process. EIS study shows that the exsolution approach improves the adsorption of gaseous species compared to LSCM. The symmetrical cell with  $\text{LSC}_{0.4}\text{MRu}_{0.1}$  as anode material exhibits an  $R_p$  as low as  $0.087 \Omega \cdot \text{cm}^2$  at 600 °C. Under methane, the comparison of the proportion of the different contributions to the polarization resistance seems to point towards a better behavior of  $\text{LSC}_{0.4}\text{MRu}_{0.1}$  towards oxidation of  $\text{CH}_4$  compared to  $\text{LSCM}_{0.3}\text{Ni}_{0.2}$ . Finally, it is important to state that it is difficult to compare phases with exsolved particles with the phases from which they are issued since the substitution of metallic oxide also changes the intrinsic properties of the phase.

### **Acknowledgements**

This study was financially supported by the Direction Générale de l'Armement (DGA) and the region Pays de la Loire. Thanks to Odile Bohnke for the electron-blocking measurements and Jonathan Hamon for XPS measurements. Many thanks to Guilhem Dezanneau for proofreading.

### **References**

- [1] D. Udomsilp, J. Rechberger, R. Neubauer, C. Bischof, F. Thaler, W. Schafbauer, N.H. Menzler, L.G.J. de Haart, A. Nenning, A.K. Opitz, O. Guillon, M. Bram, Metal-Supported Solid Oxide Fuel Cells with Exceptionally High Power Density for Range Extender Systems, *Cell Reports Phys. Sci.* 1 (2020) 100072. <https://doi.org/10.1016/j.xcrp.2020.100072>.
- [2] D. Udomsilp, C. Lenser, O. Guillon, N.H. Menzler, Performance Benchmark of Planar Solid Oxide Cells Based on Material Development and Designs, *Energy Technol.* (2021) 2001062. <https://doi.org/10.1002/ente.202001062>.

- [3] Benamira M, Ringuedé A, Cassir M, Horwat D, Lenormand P, Ansart F, et al. Enhancing oxygen reduction reaction of YSZ/La<sub>2</sub>NiO<sub>4+δ</sub> using an ultrathin La<sub>2</sub>NiO<sub>4+δ</sub> interfacial layer. *J Alloys Compd* 2018;746:413–20. <https://doi.org/10.1016/j.jallcom.2018.02.339>.
- [4] Benamira M, Letilly M, Quarez E, Joubert O, Le Gal La Salle A. Optimization of SOFC anode/electrolyte assembly based on BaIn<sub>0.3</sub>Ti<sub>0.7</sub>O<sub>2.85</sub> (BIT07)/Ni-BIT07 using an interfacial anodic layer. *J Power Sources* 2014; 251: 66–74.
- [5] Benamira M, Niinistö L, Ringuedé A, Cassir M. India-doped zirconia multi-layered thin film synthesized by atomic layer deposition for IT-SOFCs: Synthesis and electrochemical properties. *Mater Chem Phys* 2020; 241: 122386. <https://doi.org/10.1016/j.matchemphys.2019.122386>.
- [6] M. Xu, J. Yu, Y. Song, R. Ran, W. Wang, Z. Shao, *Advances in Ceramic Thin Films Fabricated by Pulsed Laser Deposition for Intermediate-Temperature Solid Oxide Fuel Cells*, *Energy & Fuels*. 34 (2020) 10568–10582.
- [7] Lay E, Benamira M, Pirovano C, Gauthier G, Dessemond L. Effect of Ce-doping on the electrical and electrocatalytical behavior of La/Sr chromo-manganite perovskite as new SOFC anode. *Fuel Cells*, vol. 12, 2012, p. 265–74. <https://doi.org/10.1002/fuce.201100070>.
- [8] Y. Su, T. Wei, Y. Li, B. Yin, Y. Huan, D. Dong, X. Hu, B. Huang, A highly active CH<sub>4</sub>catalyst correlated with solid oxide fuel cell anode performance, *J. Mater. Chem. A*. 9 (2021) 5067–5074. <https://doi.org/10.1039/d0ta10672k>.
- [9] Benamira M, Thommy L, Moser F, Joubert O, Caldes MT. New anode materials for IT-SOFC derived from the electrolyte BaIn<sub>0.3</sub>Ti<sub>0.7</sub>O<sub>2.85</sub> by lanthanum and manganese doping. *Solid State Ionics* 2014;265:38–45. <https://doi.org/10.1016/j.ssi.2014.07.006>.
- [10] S. Futamura, A. Muramoto, Y. Tachikawa, J. Matsuda, S.M. Lyth, Y. Shiratori, S. Taniguchi, K. Sasaki, SOFC anodes impregnated with noble metal catalyst nanoparticles for high fuel utilization, *Int. J. Hydrogen Energy*. 44 (2019) 8502–8518. <https://doi.org/10.1016/j.ijhydene.2019.01.223>.
- [11] Moser F, Caldes MT, Benamira M, Greneche JM, Leone P, Joubert O. Development of new anodes compatible with the solid oxide fuel cell electrolyte BaIn<sub>0.3</sub>Ti<sub>0.7</sub>O<sub>2.85</sub>. *J Power Sources* 2012;201:103–11. <https://doi.org/10.1016/j.jpowsour.2011.10.120>.
- [12] Primdahl S, Mogensen M. Mixed conductor anodes: Ni as electrocatalyst for hydrogen conversion. *Solid State Ionics* 2002;152:597–608.

- [13] Hibino T, Hashimoto A, Yano M, Suzuki M, Sano M. Ru-catalyzed anode materials for direct hydrocarbon SOFCs. *Electrochim Acta* 2003;48:2531–7. [https://doi.org/10.1016/S0013-4686\(03\)00296-2](https://doi.org/10.1016/S0013-4686(03)00296-2).
- [14] Caldes MT, Kravchyk K V., Benamira M, Besnard N, Joubert O, Bohnke O, et al. Metallic Nanoparticles and Proton Conductivity: Improving Proton Conductivity of  $\text{BaCe}_{0.9}\text{Y}_{0.1}\text{O}_{3-\delta}$  and  $\text{La}_{0.75}\text{Sr}_{0.25}\text{Cr}_{0.5}\text{Mn}_{0.5}\text{O}_{3-\delta}$  by Ni-doping. *ECS Trans* 2012;45:143–54. <https://doi.org/10.1149/1.3701303>.
- [15] Bartholomew CH. Carbon Deposition in Steam Reforming and Methanation. *Catal Rev* 1982;24:67–112. <https://doi.org/10.1080/03602458208079650>.
- [16] Sauvet A-L, Fouletier J, Gaillard F, Primet M. Surface properties and physicochemical characterizations of a new type of anode material,  $\text{La}_{1-x}\text{Sr}_x\text{Cr}_{1-y}\text{Ru}_y\text{O}_{3-\delta}$ , for a solid oxide fuel cell under methane at intermediate temperature. *J Catal* 2002;209:25–34.
- [17] Gorte RJ, Vohs JM, McIntosh S. Recent developments on anodes for direct fuel utilization in SOFC. *Solid State Ionics* 2004;175:1–6.
- [18] Thommy L, Joubert O, Hamon J, Caldes M-T. Impregnation versus exsolution: Using metal catalysts to improve electrocatalytic properties of LSCM-based anodes operating at 600 C. *Int J Hydrogen Energy* 2016;41:14207–16.
- [19] Kobsiriphat W, Madsen BD, Wang Y, Shah M, Marks LD, Barnett SA. Nickel-and ruthenium-doped lanthanum chromite anodes: effects of nanoscale metal precipitation on solid oxide fuel cell performance. *J Electrochem Soc* 2010;157:B279–84.
- [20] Madsen BD, Kobsiriphat W, Wang Y, Marks LD, Barnett SA. Nucleation of nanometer-scale electrocatalyst particles in solid oxide fuel cell anodes. *J Power Sources* 2007;166:64–7.
- [21] Neagu D, Tsekouras G, Miller DN, Ménard H, Irvine JTS. In situ growth of nanoparticles through control of non-stoichiometry. *Nat Chem* 2013;5:916–23.
- [22] Katz MB, Zhang S, Duan Y, Wang H, Fang M, Zhang K, et al. Reversible precipitation/dissolution of precious-metal clusters in perovskite-based catalyst materials: Bulk versus surface re-dispersion. *J Catal* 2012;293:145–8.
- [23] Nishihata Y, Mizuki J, Akao T, Tanaka H, Uenishi M, Kimura M, et al. Self-regeneration of a Pd-perovskite catalyst for automotive emissions control. *Nature* 2002;418:164–7. <https://doi.org/10.1038/nature00893>.

- [24] Kim J-S, Wieder NL, Abraham AJ, Cargnello M, Fornasiero P, Gorte RJ, et al. Highly Active and Thermally Stable Core-Shell Catalysts for Solid Oxide Fuel Cells. *J Electrochem Soc* 2011;158:B596. <https://doi.org/10.1149/1.3571039>.
- [25] Tauster SJ. Strong metal-support interactions. *Acc Chem Res* 1987;20:389–94.
- [26] S. Tao, J.T.S. Irvine, A redox-stable efficient anode for solid-oxide fuel cells, *Nat. Mater.* 2 (2003) 320–323. <https://doi.org/10.1038/nmat871>.
- [27] S. Tao, J.T.S. Irvine, Synthesis and Characterization of  $(\text{La}_{0.75}\text{Sr}_{0.25})\text{Cr}_{0.5}\text{Mn}_{0.5}\text{O}_{3-\delta}$ , a Redox-Stable, Efficient Perovskite Anode for SOFCs, *J. Electrochem. Soc.* 151 (2004) A252. <https://doi.org/10.1149/1.1639161>.
- [28] Ruiz-Morales JC, Canales-Vázquez J, Peña-Martínez J, López DM, Núñez P. On the simultaneous use of  $\text{La}_{0.75}\text{Sr}_{0.25}\text{Cr}_{0.5}\text{Mn}_{0.5}\text{O}_{3-\delta}$  as both anode and cathode material with improved microstructure in solid oxide fuel cells. *Electrochim Acta* 2006;52:278–84.
- [29] Jardiel T, Caldes MT, Moser F, Hamon J, Gauthier G, Joubert O. New SOFC electrode materials: The Ni-substituted LSCM-based compounds  $(\text{La}_{0.75}\text{Sr}_{0.25})(\text{Cr}_{0.5}\text{Mn}_{0.5-x}\text{Ni}_x)\text{O}_{3-\delta}$  and  $(\text{La}_{0.75}\text{Sr}_{0.25})(\text{Cr}_{0.5-x}\text{Ni}_x\text{Mn}_{0.5})\text{O}_{3-\delta}$ . *Solid State Ionics* 2010;181:894–901.
- [30] Rodríguez-Carvajal J. Recent advances in magnetic structure determination by neutron powder diffraction. *Phys B Phys Condens Matter* 1993;192:55–69.
- [31] Zipprich W, Wiemhöfer HD. Measurement of ionic conductivity in mixed conducting compounds using solid electrolyte microcontacts. *Solid State Ionics* 2000;135:699–707.
- [32] S.S. Manoharan, R.K. Sahu, Evidence for an anomalous redox ionic pair between Ru and Mn in  $\text{SrRu}_{0.5}\text{Mn}_{0.5}\text{O}_3$ : An X-ray absorption spectroscopy approach, *Chem. Commun.* (2002) 3068–3069.
- [33] Kharton V V., Tsipis E V., Marozau IP, Viskup AP, Frade JR, Irvine JTS. Mixed conductivity and electrochemical behavior of  $(\text{La}_{0.75}\text{Sr}_{0.25})_{0.95}\text{Cr}_{0.5}\text{Mn}_{0.5}\text{O}_{3-\delta}$ . *Solid State Ionics* 2007;178:101–13.
- [34] Beyreuther E, Grafström S, Eng LM, Thiele C, Dörr K. XPS investigation of Mn valence in lanthanum manganite thin films under variation of oxygen content. *Phys Rev B - Condens Matter Mater Phys* 2006;73:155425.
- [35] Shen JY, Adnot A, Kaliaguine S. An ESCA study of the interaction of oxygen with the surface of ruthenium. *Appl Surf Sci* 1991;51:47–60.

- [36] S. Tao, J.T.S. Irvine, Phase transition in perovskite oxide  $\text{La}_{0.75}\text{Sr}_{0.25}\text{Cr}_{0.5}\text{Mn}_{0.5}\text{O}_{3-\delta}$  observed by in situ high-temperature neutron powder diffraction, *Chem. Mater.* 18 (2006) 5453–5460. <https://doi.org/10.1021/cm061413n>.
- [37] Bashir J, Shaheen R, Khan MN. Structural characterization of  $\text{SrLaMnRuO}_6$  by synchrotron X-ray powder diffraction and X-ray absorption spectroscopy. *Solid State Sci* 2008;10:638–44..
- [38] Rath MK, Choi BH, Lee KT. Properties and electrochemical performance of  $\text{La}_{0.75}\text{Sr}_{0.25}\text{Cr}_{0.5}\text{Mn}_{0.5}\text{O}_{3-\delta}$ - $\text{La}_{0.2}\text{Ce}_{0.8}\text{O}_{2-\delta}$  composite anodes for solid oxide fuel cells. *J Power Sources* 2012;213:55–62.
- [39] E. Lay, L. Dessemond, G. Gauthier, Ba-substituted LSCM anodes for solid oxide fuel cells, *J. Power Sources.* 221 (2013) 149–156.
- [40] S. Zhang, Y. Wan, Z. Xu, S. Xue, L. Zhang, B. Zhang, C. Xia, Bismuth doped  $\text{La}_{0.75}\text{Sr}_{0.25}\text{Cr}_{0.5}\text{Mn}_{0.5}\text{O}_{3-\delta}$  perovskite as a novel redox-stable efficient anode for solid oxide fuel cells, *J. Mater. Chem. A.* 8 (2020) 11553–11563.
- [41] A. Ghosh, A. Azad, J.T. Irvine, Study of Ga Doped LSCM as an Anode for SOFC, *ECS Trans.* 35 (2011) 1337.
- [42] P. Blennow, J. Hjelm, T. Klemensø, A. Persson, K. Brodersen, A. Srivastava, H. Frandsen, M. Lundberg, S. Ramousse, M. Mogensen, Development of planar metal supported SOFC with novel cermet anode, *ECS Trans.* 25 (2009) 701.
- [43] T. Zhu, H.E. Troiani, L. V Mogni, M. Han, S.A. Barnett, Ni-Substituted  $\text{Sr}(\text{Ti},\text{Fe})\text{O}_3$  SOFC Anodes: Achieving High Performance via Metal Alloy Nanoparticle Exsolution, *Joule.* 2 (2018) 478–496. <https://doi.org/https://doi.org/10.1016/j.joule.2018.02.006>.
- [44] C.D. Savaniu, J.T.S. Irvine, La-doped  $\text{SrTiO}_3$  as anode material for IT-SOFC, *Solid State Ionics.* 192 (2011) 491–493. <https://doi.org/https://doi.org/10.1016/j.ssi.2010.02.010>.
- [45] Ferreira-Aparicio P, Rodríguez-Ramos I, Anderson JA, Guerrero-Ruiz A. Mechanistic aspects of the dry reforming of methane over ruthenium catalysts. *Appl Catal A Gen* 2000;202:183–96.
- [46] N.K. Labhsetwar, A. Watanabe, T. Mitsuhashi, H. Haneda, Thermally stable ruthenium-based catalyst for methane combustion, *J. Mol. Catal. A Chem.* 223 (2004) 217–223.

## Table captions

**Table 1:** Results of XPS experiments: Ru 3p<sub>3/2</sub> and Mn 3s energy splitting of the different materials studied and some literature references, along with the corresponding valence calculated with eq. (1).

**Table 2:** Calculated values of the  $R_p$  and its different contributions at 600 °C under wet Ar/H<sub>2</sub> (5%), obtained from fitting the impedance with the equivalent circuit proposed.

**Table 3:** Calculated values of the  $R_p$  and its different contributions under methane at 600 °C, obtained from fitting the impedance with the equivalent circuit proposed.

**Table 4:** typical reported polarization resistance of A-site and B-site doped LSCM, STF<sub>N</sub> and LSC anode materials.

## Figure Captions

**Fig. 1:** (a) Representation of the O<sup>2-</sup> conductivity setup using an electron-blocking microelectrode. (b) Refined XRD pattern of LSC<sub>0.4</sub>MRu<sub>0.1</sub> obtained by combustion method and calcined at 1000 °C/12h. Difference between the observed (•) and calculated profiles (solid lines) is plotted at the bottom in blue. Green ticks indicate the position of the calculated Bragg reflections.

**Fig. 2:** Evolution of the total conductivity of LSC<sub>0.4</sub>MRu<sub>0.1</sub>, LSCM<sub>0.3</sub>Ni<sub>0.2</sub> and LSCM upon cooling at 50 °C h<sup>-1</sup> under (a) dry air and (b) wet Ar/H<sub>2</sub> (5%), (c) O<sup>2-</sup> ionic conductivity of LSC<sub>0.4</sub>MRu<sub>0.1</sub> as function of oxygen activity at the surface of the microcontact at different temperatures.

**Fig. 3:** Background-subtracted XPS spectra of (a) Ru 3p<sub>3/2</sub> core level and (b) Mn 3s core level of different compounds.

**Fig. 4:** (a) XRD patterns of LSCM<sub>0.3</sub>Ni<sub>0.2</sub>, before and after reduction at 800 °C under Ar/H<sub>2</sub> (5%) (b) Structural transition and evolution of the cell parameters of LSCM<sub>0.3</sub>Ni<sub>0.2</sub> with the temperature under N<sub>2</sub>/H<sub>2</sub> (5%), heating to 750 °C and cooling down to room T °C, with the deviation to the cubicity. (c) SEM and (d) TEM image of the surface

of  $\text{LSCM}_{0.3}\text{Ni}_{0.2}$  reduced under  $\text{Ar}/\text{H}_2$  (5%) for 12h.

**Fig. 5:** (a) Evolution of the cell parameters of  $\text{LSCM}_{0.3}\text{Ni}_{0.2}$  with the temperature, with the deviation to the cubicity (b) XRD patterns of  $\text{LSC}_{0.4}\text{MRu}_{0.1}$ , before and after reduction at different temperatures under  $\text{Ar}/\text{H}_2$  (5%) (c) TEM and (d) SEM images of the surface of  $\text{LSC}_{0.4}\text{MRu}_{0.1}$  after reduction at  $1000\text{ }^\circ\text{C}/12\text{h}$ .

**Fig. 6:** XRD pattern of  $\text{LSC}_{0.4}\text{MRu}_{0.1}$  after each step of the thermal treatment used in the fabrication of symmetrical cells.

**Fig. 7:** Nyquist plot of the impedance obtained at  $600\text{ }^\circ\text{C}$  under wet  $\text{Ar}/\text{H}_2$  (5%) for (a)  $\text{LSCM}$ -, (b)  $\text{LSC}_{0.4}\text{MRu}_{0.1}$ - and (c)  $\text{LSCM}_{0.3}\text{Ni}_{0.2}$ -based symmetrical cell, fitted with the equivalent circuit (d) proposed and subtracted from  $R_s$ .

**Fig. 8:** (a) Cross sectional SEM image of a  $\text{Ni}/\text{LSCM}/\text{CGO}/\text{LSCM}/\text{Ni}$  symmetrical cell along with details of the cells electrodes based on (b,c)  $\text{LSCM}$  (d,e)  $\text{LSC}_{0.4}\text{Ru}_{0.1}$  (f,g)  $\text{LSCM}_{0.3}\text{Ni}_{0.2}$  after EIS measurements.

**Fig. 9:** Nyquist plot of the impedance obtained at  $600\text{ }^\circ\text{C}$  under wet pure  $\text{CH}_4$  for (a)  $\text{LSC}_{0.4}\text{MRu}_{0.1}$ - and (b)  $\text{LSCM}_{0.3}\text{Ni}_{0.2}$ -based symmetrical cell, fitted with the equivalent circuit proposed in Fig. 7d and subtracted from  $R_s$ .

**Table 1**

$\Delta E_{3s}$	$V_{Mn}$	Compound	Ru 3p <sub>3/2</sub> (eV)
4.8	3.6	LSCM	
4.9	3.4	LSC <sub>0.4</sub> MRu <sub>0.1</sub> as prepared	464.8
5.4	2.8	LSC <sub>0.4</sub> MRu <sub>0.1</sub> red. at 800°C	462.1
5.3	2.9	Mn <sub>2</sub> O <sub>3</sub>	
		RuO <sub>2</sub> (This work)	463.7
		RuO <sub>2</sub> (literature) [26]	462.3- 463.2
		Ru <sup>0</sup> (This work)	461.46

**Table 2**

Material	$\sigma_{elec}$ (S.cm <sup>-1</sup> )	$Rp$ ( $\Omega$ .cm <sup>2</sup> )	$f_1$ (Hz)	$C_1$ (F.cm <sup>-2</sup> )	$Rp_1$ ( $\Omega$ .cm <sup>2</sup> )	$f_2$ (Hz)	$C_2$ (F.cm <sup>-2</sup> )	$Rp_2$ ( $\Omega$ .cm <sup>2</sup> )
LSCM	$2,6 \cdot 10^{-2}$	0.20(1)	3000	$3.7 \cdot 10^{-4}$	0.072(7)	447	$1.4 \cdot 10^{-3}$	0.127(7)
LSC <sub>0.4</sub> MRu <sub>0.1</sub>	$2.4 \cdot 10^{-2}$	0.087(4)	2287	$1.1 \cdot 10^{-3}$	0.038(2)	666	$2.9 \cdot 10^{-3}$	0.049(2)
LSCM <sub>0.3</sub> Ni <sub>0.2</sub>	$2.8 \cdot 10^{-2}$	0.20(1)	3862	$2.0 \cdot 10^{-5}$	0.105(5)	1348	$6.0 \cdot 10^{-4}$	0.098(5)

**Table 3**

Electrode Material	$\sigma_{elec}$ (S.cm <sup>-1</sup> )	$Rp$ ( $\Omega$ .cm <sup>2</sup> )	$f_1$ (Hz)	$C_1$ (F)	$Rp_1$ ( $\Omega$ .cm <sup>2</sup> )	$f_2$ (Hz)	$C_2$ (F)	$Rp_2$ ( $\Omega$ .cm <sup>2</sup> )
LSCM <sub>0.3</sub> Ni <sub>0.2</sub>	$5.24 \cdot 10^{-3}$	0.124(6)	31850	$9.10 \cdot 10^{-5}$	0.055(3)	1804	$1.28 \cdot 10^{-3}$	0.069(3)
LSC <sub>0.4</sub> MRu <sub>0.1</sub>	$2.46 \cdot 10^{-2}$	0.044(2)	30863	$2.09 \cdot 10^{-4}$	0.023(1)	6166	$1.23 \cdot 10^{-3}$	0.021(1)

**Table 4**

Composition	T (°C)	R <sub>p</sub> (Ω cm <sup>2</sup> )	Oxidant	Electrolyte	Ref
LSCM <sub>0.3</sub> Ni <sub>0.2</sub>	600	0.087	Ar/H <sub>2</sub> (5%)	CGO	this work
LSC0.4MRu0.1	600	0.044	CH <sub>4</sub>	CGO	this work
Ce-LSCM	800	0.11	H <sub>2</sub> -3% H <sub>2</sub> O	YSZ	7
Ba-LSCM	800	5	H <sub>2</sub> -3% H <sub>2</sub> O	YSZ	39
Bi-LSCM	800	1.04	wet 5% H <sub>2</sub> -Ar	LSGM	40
Ga-LSCM	850	0.69	wet 5% H <sub>2</sub>	YSZ	41
Cu-LSCM	900	0.38	wet 5% H <sub>2</sub> -Ar	YSZ	8
CGO20-Ni	650	0.12	wet H <sub>2</sub> - N <sub>2</sub>	YSZ	42
Sr <sub>0.95</sub> (Ti <sub>0.3</sub> Fe <sub>0.63</sub> Ni <sub>0.07</sub> )O <sub>3-δ</sub>	800	0.21	3% H <sub>2</sub> O/H <sub>2</sub> -Ar	LSGM	43
La <sub>0.6</sub> Sr <sub>0.4</sub> CoO <sub>3</sub>	750	0.53	wet 5% H <sub>2</sub> -Ar	YSZ	44

# Figures

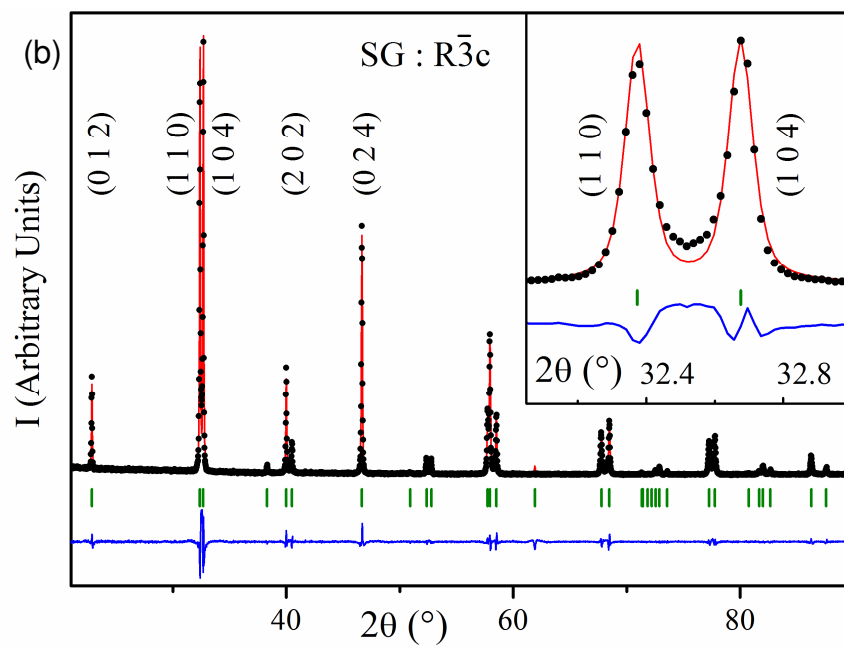
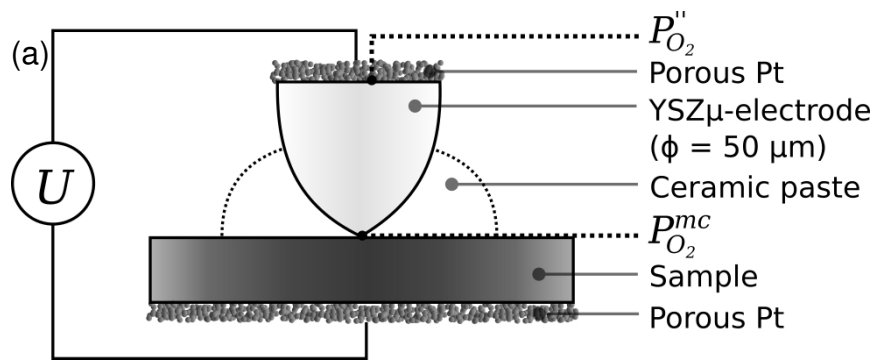


Figure 1

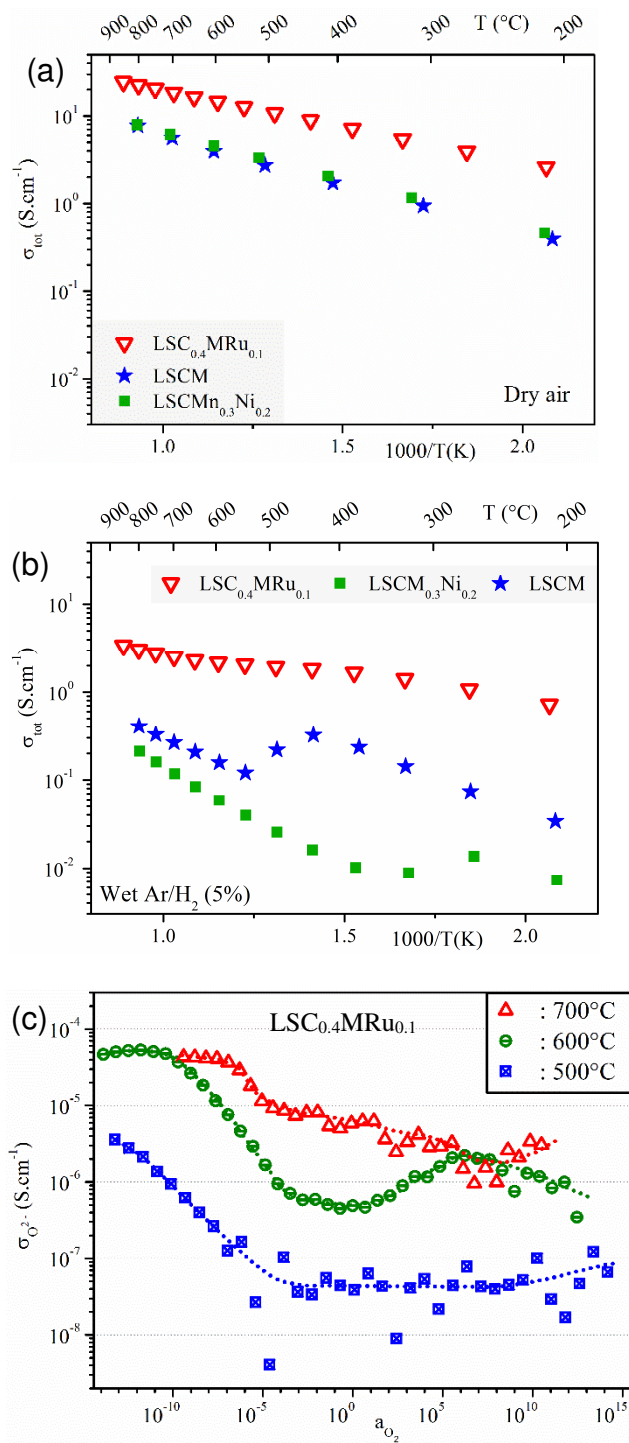


Figure 2

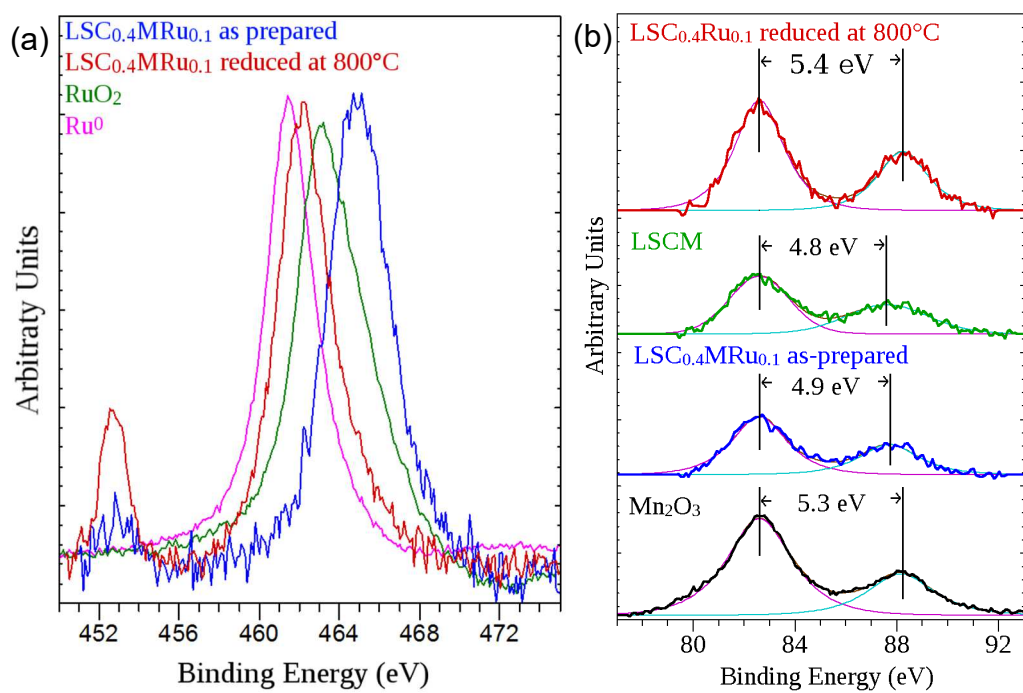


Figure 3

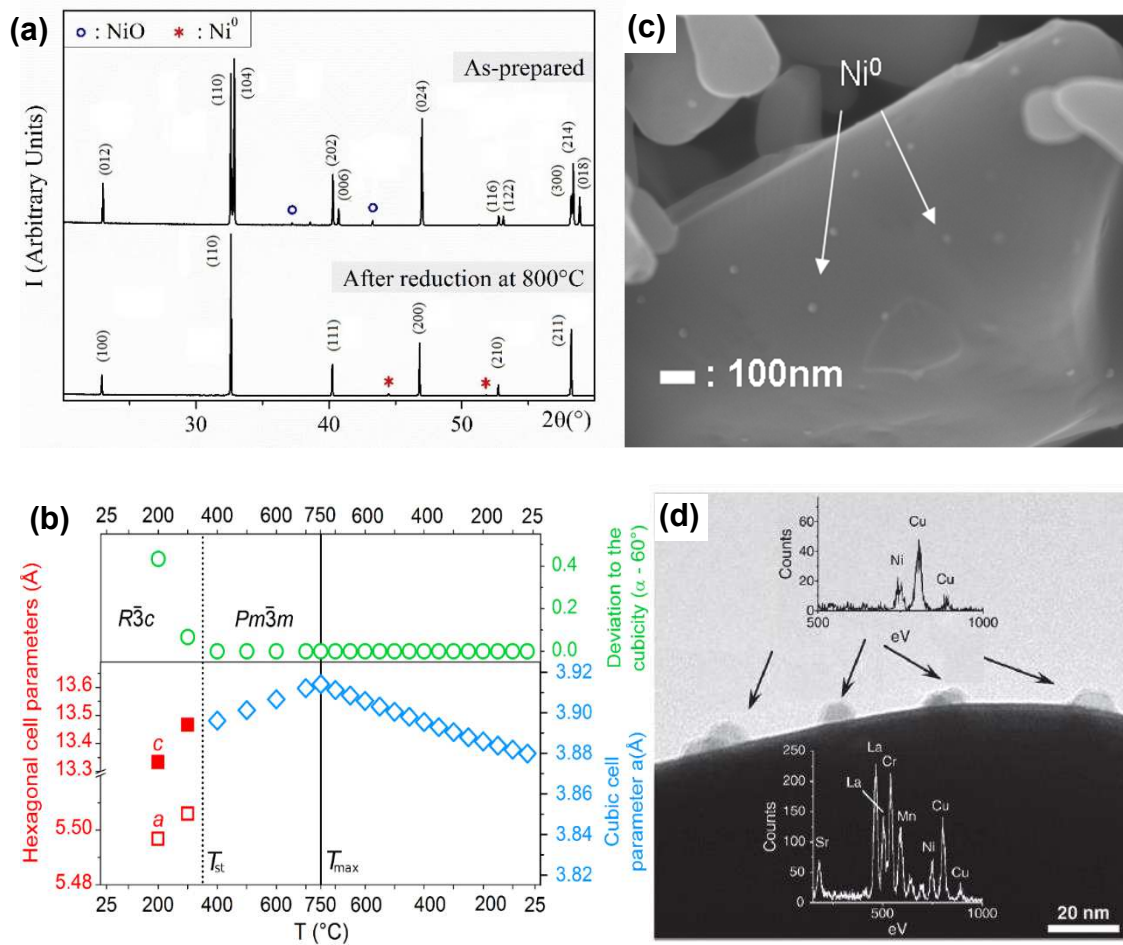


Figure 4

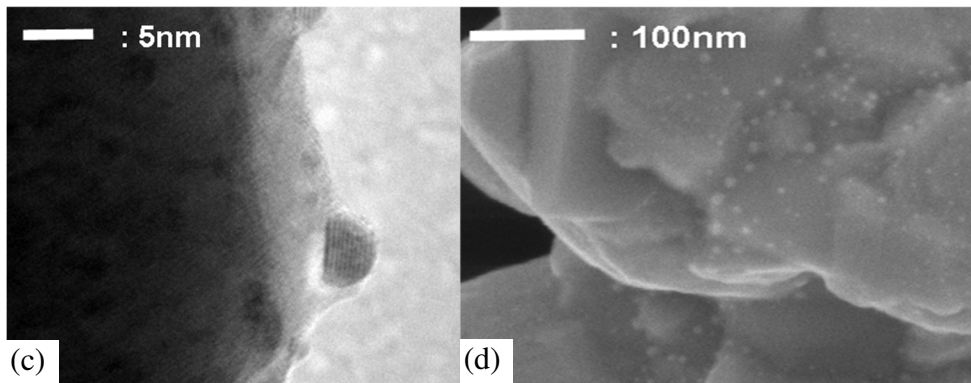
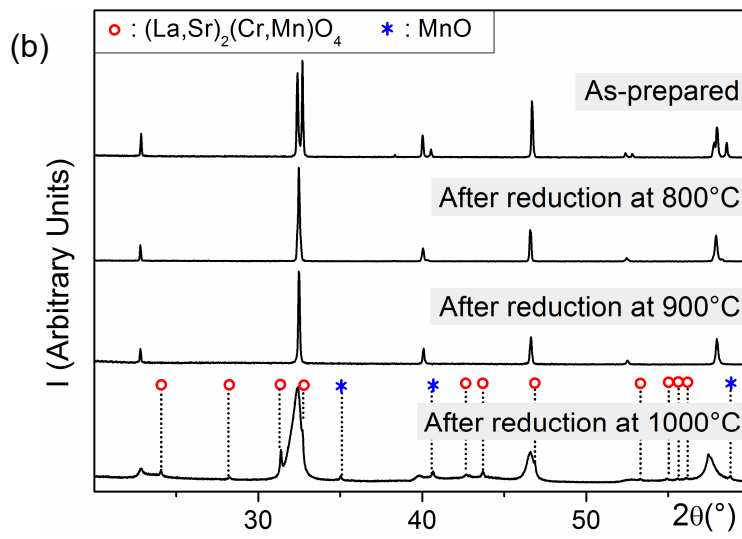
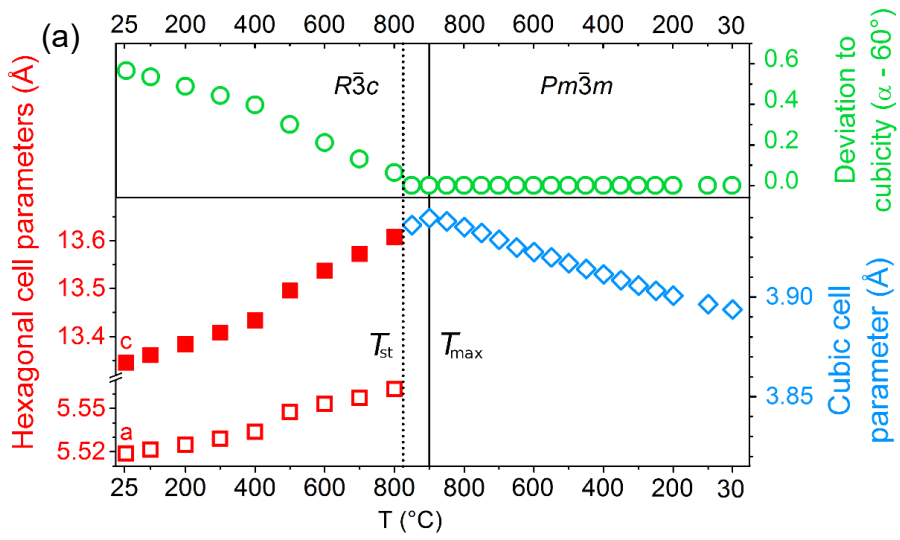


Figure 5

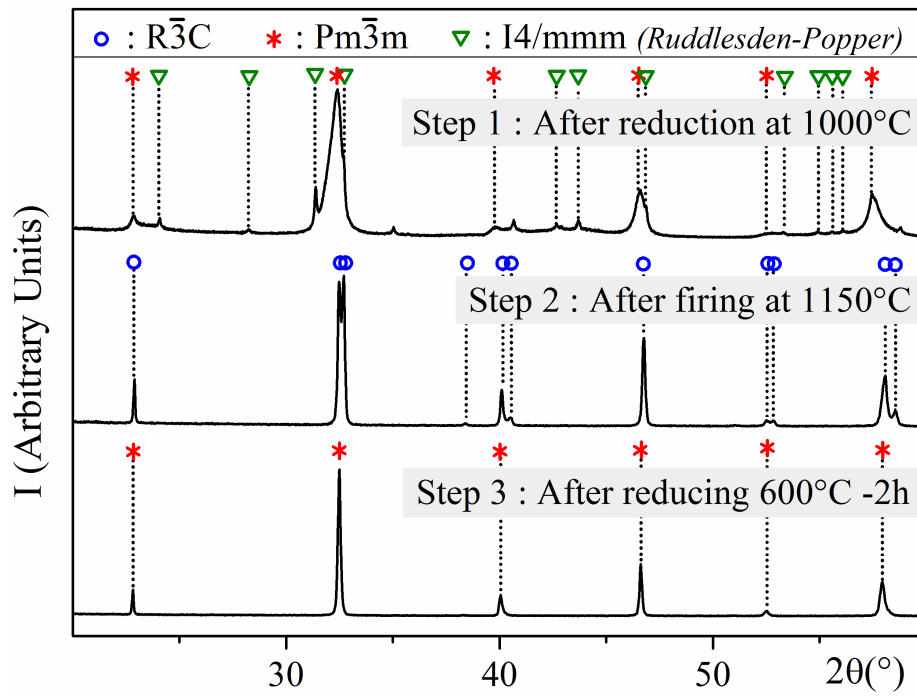


Figure 6

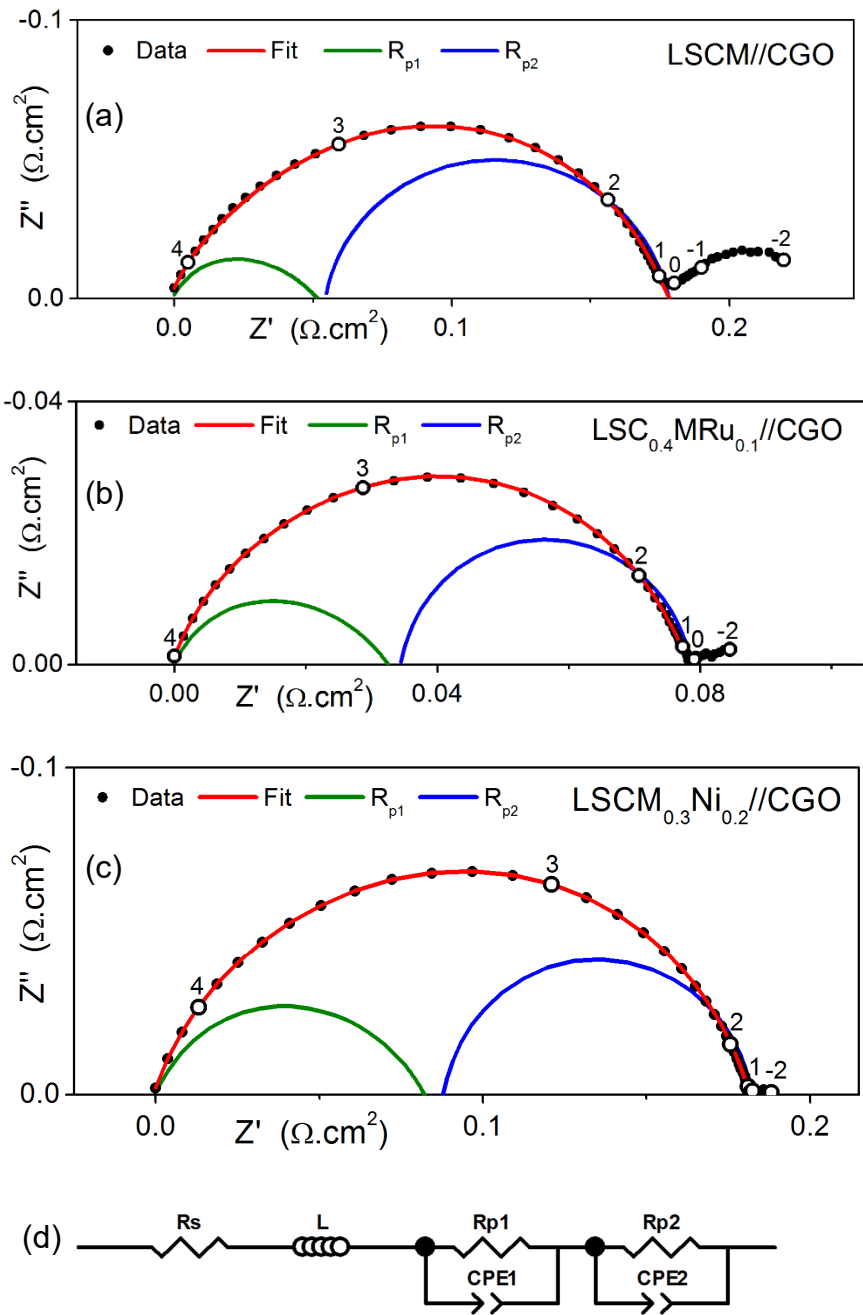


Figure 7

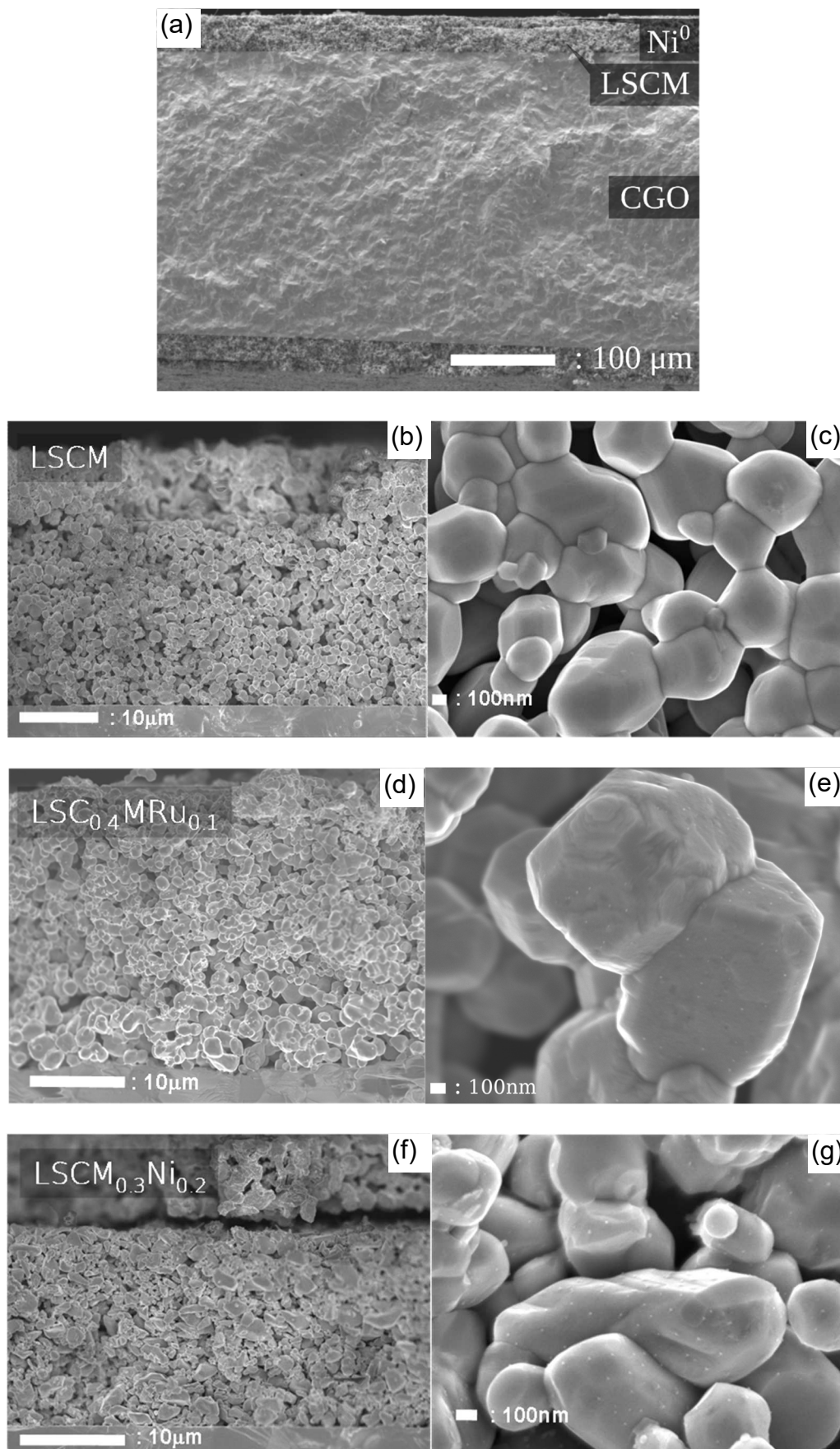


Figure 8

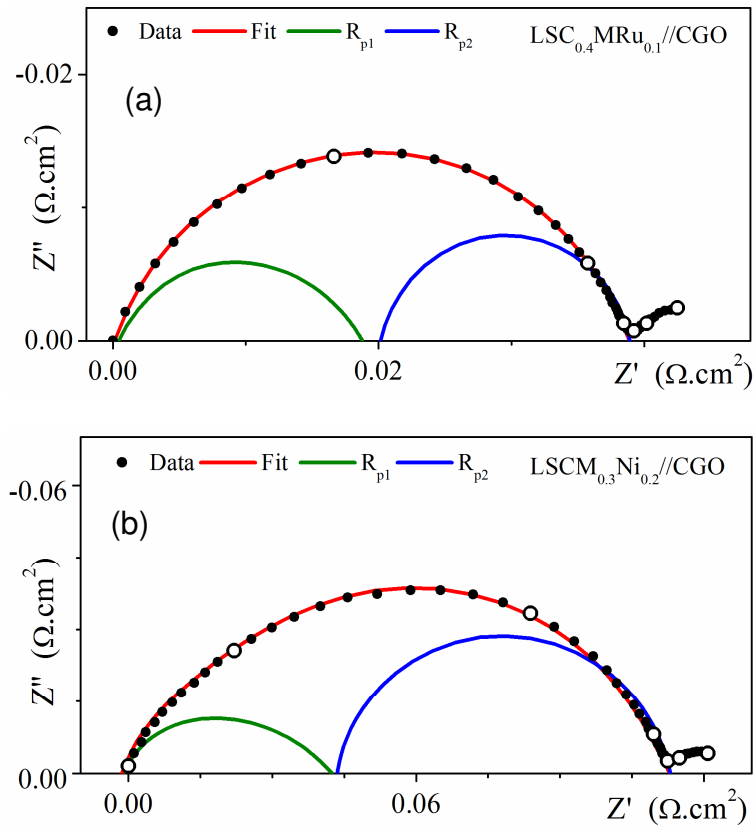


Figure 9

## Graphical Abstract

